Journal of The Electrochemical Society, **156** (3) B403-B409 (2009)
0013-4651/2009/156(3)/B403/7/$23.00 © The Electrochemical Society

Analysis of the Reaction Rates in the Cathode Electrode of Polymer Electrolyte Fuel Cells

II. Dual-Layer Electrodes

Yun Wang[*,z] **and Xuhui Feng**

Renewable Energy Resources Lab (RERL) and National Fuel Cell Research Center, Department of Mechanical and Aerospace Engineering, The University of California, Irvine, Irvine, California 92697-3975, USA

This paper presents a one-dimensional (1D) theoretical study on the electrochemical phenomena in the cathode dual-layer electrode of polymer electrolyte fuel cells (PEFCs). Following our previous work on transport and electrochemical processes in single-layer cathodes [Y. Wang and X. H. Feng, *J. Electrochem. Soc.*, **155**, B1289 (2008)], we extend the analysis to dual-layer catalyst layers, where the electrode is characterized by a two-layer configuration with specific properties assigned to each layer. A 1D model is developed, and explicit solutions are obtained for the profiles of the reaction rate and electrolyte phase potential across the dual-layer electrode. Effort is also made to analyze the solutions to explore the impacts of each layer's properties on their performance (i.e., the average reaction current in each layer) with particular focus on the ratios of the ionic conductivity (related to the ionomer content), specific area, and exchange current density (related to Pt loading and reaction interface roughness). The results can be applied to optimize electrode performance through dual-layer configuration for high-performance cost-effective electrodes for PEFCs.
 [DOI: 10.1149/1.3056057]

Manuscript submitted September 17, 2008; revised manuscript received November 26, 2008. Published January 21, 2009.

The cathode electrode or catalyst layer plays a vital role in the operation of a polymer electrolyte fuel cell (PEFC). In the cathode, the electrochemical reaction of oxygen reduction takes place at the boundaries of the triple phases (i.e., gas, ionomer, and electrochemical catalyst). The reaction activity within the electrode is closely related to the local electrode structure and composition as well as species transport characteristics. Understanding the local electrode process and performance is of vital importance to electrode optimization (e.g., catalyst Pt loading reduction). Introductions to the electrode functions, preparation, catalysts, and fundamental modeling for PEFCs are given by Ref. 1-4.

Electrode optimization is a central topic in PEFC development. Ticianelli et al.[5] discussed three methods to explore relatively thin catalyst layers for Pt loading reduction. Their results indicated that sputtering a Pt film on the electrode surface may substantially increase cell power densities. Mukerjee et al.[6] further explored the impact of sputtered Pt film on the performance of low Pt-loading electrodes. Antoine et al.[7] present a study on the influence of Pt loading on the cathode performance. Modeling predictions were also conducted to explain the experimental observations. Their results indicated that the optimal catalyst utilization may be obtained through a thin porous active layer and a preferential location of Pt nanoparticles near the membrane. Passalacqua et al.[8] experimentally explored the impacts of the electrode structure and composition on fuel cell performance. Antolini et al.[9] focused on the effect of the Nafion loading on electrode performance. An optimum value of the Nafion loading was identified in their case. Madhusudana Rao and Rengaswamy[10] employed a spherical agglomerate model to optimize the Pt loading and ionomer content in the cathode. They considered three optimization formulations and concluded that a graded distribution of platinum may improve Pt utilization. Song et al.[11] conducted a numerical study on optimizing four parameters such as the Nafion and Pt loadings for PEFC cathodes. Their results indicated that the cathode performance is also sensitive to the electrode thickness. Their following paper[12] further focused on Pt and ionomer loadings for cell-performance optimization. Boyer et al.[13] presented a simple mathematical expression for fuel cell electrode optimization. They investigated the effects of the electrode thickness, Nafion content, and catalyst loading. Das et al.[14] developed a fuel cell model to relate the electrode parameters to cell performance and investigated the impacts of platinum loading and electrode thickness. Lee and Hwang[15] explored the ionomer content distributions in the catalyst layer to optimize electrode performance. Mukherjee and Wang[16] proposed direct numerical simulations to investigate species transport within the catalyst layer. They employed a stochastic reconstruction technique to generate a bilayer catalyst layer with different porosities and Nafion contents. In our previous paper,[17] we explicitly obtain the reaction rate profile within a single-layer electrode. A considerable spatial variation of reaction rates across the electrode was reported, and a parameter $\hbar$ was defined to quantify the degree of reaction spatial variation (see Fig. 1), which implies that the overall performance and electrode catalyst utilization may be enhanced through optimizing local electrode activities and properties.

In this paper, we follow our previous theoretical analysis on a single-layer electrode[17] and extend the explicit theoretical solutions to a more complicated configuration (i.e., the dual-layer electrode), which allows specific properties assigned to different layers and hence the electrode optimization through adjusting the two layers'

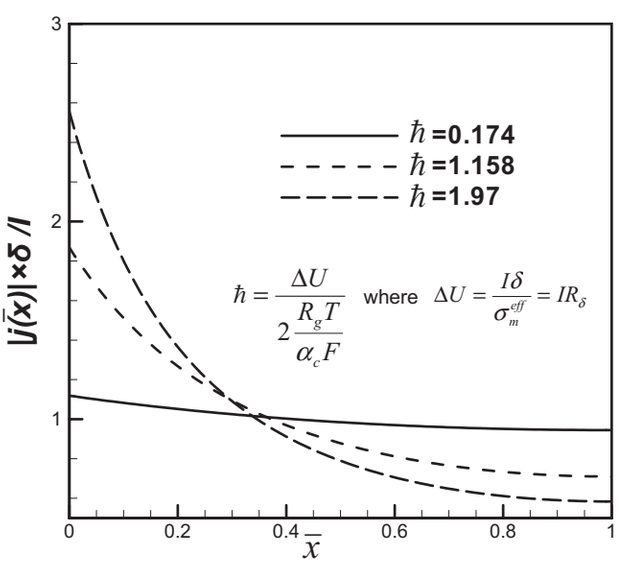

Figure 1. Spatial variation of the reaction current densities at different $\hbar$.[17]

* Electrochemical Society Active Member.
[z] E-mail: yunw@uci.edu

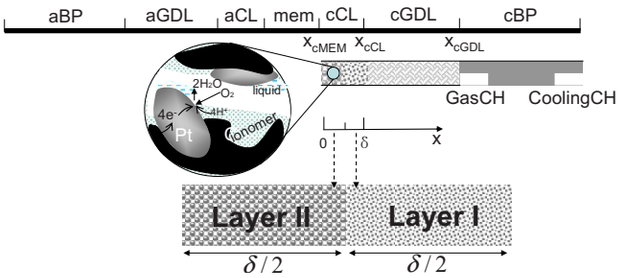

Figure 2. (Color online) Schematic of the dual-layer cathode electrode in a PEFC.

properties. The profiles of the key quantities, such as the electrolyte phase potential and reaction rate within the bilayer electrode, are explicitly obtained. Analysis is also performed on the average performance of each layer and impacts of the properties, such as the ionic conductivity (related to the ionomer content), active surface, and exchange current density (related to the reaction interface roughness and Pt loading) that characterize the bilayer configuration. We also develop the direct relations between the ratios of these key parameters in the two layers and the ratios of the two layers' performances and catalyst utilizations.

Theoretical Analysis and Modeling

Figure 2 displays the schematics of the dual-layer electrode in a PEFC. The left side of the electrode attaches the polymer electrolyte membrane, while the right connects to the diffusion media. There are three phases, in addition to the electrochemical catalyst, in the electrode that are necessary for its functions: (*i*) the void space for gaseous reactant transport, (*ii*) ionomer content for protons transfer, and (*iii*) carbon support for electronic current conduction. The dual-layer electrode is characterized by two equal-thickness layers with specific properties assigned to each layer. For convenience, we denote these two layers by layers I and II, respectively, as shown in Fig. 2. In these two layers, we consider the following parameters that may be different, the ionic conductivity, catalyst specific surface area, and exchange current density. These parameters are directly related to the ionomer content, electrode structure (e.g., reaction interface roughness), and catalyst Pt loading that are vital to the electrode fabrication. Consequently, other parameters, such as porosity, electronic, and thermal conductivities, may vary between the layers.

Quantities that approximate unvarying between the two layers.— The electronic conductivity of the catalyst layer, though it may slightly vary from layer to layer, is typically much higher than the ionic one; therefore, the ohmic loss due to electronic resistance can be neglected across the two layers in the electrode. In addition, our previous analysis[17] on single-layer electrodes indicates that temperature and oxygen concentration variations across the catalyst layer are small and negligible. This fact still holds true in the dual-layer configuration as long as the thermal conductivity and porosity of the electrode are in the typical ranges of fuel cells. In the single-layer electrode, the effective thermal conductivity k^{eff} of 3.0 W/m K yields $\Delta T_{\text{CL}} \sim 0.03$ K within the electrode at 1.0 A/cm^2.[17] For the dual-layer electrode, the upper limit of temperature variation can be estimated through the same formula except using the smaller thermal conductivity in the two layers. Even the thermal conductivity decreases to 0.3 W/m K, this upper limit, which is reversely proportional to conductivity, is still small ~0.3 K. In addition, a more precise model can further reduce this upper limit. One can use Eq. 11 in Ref. 17 to estimate the temperature variation as heat transfer is similar to species diffusion processes, which will be reduced by half (i.e., ~0.1 K).

Likewise, the oxygen concentration variation across the dual-layer electrode can be neglected in the typical range of porosity in fuel cells: the single-layer analysis[17] indicates that $D_{\text{O}_2}^{\text{eff}}$ ($=\varepsilon^{\tau_d} D_{\text{O}_2}$, where $\varepsilon \sim 0.5$ and $\tau_d \sim 1.5$) of 10^{-5} m^2/s yields ΔC^{O_2} of ~0.02 mol/m^3 within the electrode at $I = 1.0$ A/cm^2. Even a porosity down to 0.1 or the tortuosity τ_d up to 3 still leads to a negligible oxygen concentration variation. Furthermore, liquid water may increase the transport resistance of oxygen. As shown in Ref. 17, in the range of normal liquid saturation within fuel cells (upper limit of saturation ~30 to 40%), the variation of oxygen concentration is negligibly small.

In the following analysis on dual-layer electrodes, we will assume uniform oxygen concentration and temperature across the electrode, together with spatially unvarying electronic phase potential $\Phi^{(s)}$ and equilibrium potential U_o as justified in our previous analysis.[17] Note that the above justifications are all based on typical PEFC operating conditions. For other electrochemical systems that satisfy the justifications, the analysis results to be discussed in the following are still valid.

Difference in the ionic conductivity, σ_m^{eff}.— Proton transport in the electrode takes place in the ionomer phase. The ionic conductivity of the electrode is directly related to the ionomer content, ε_{m}.[18] Other factors may also affect the ionic conductivity, and the effective ionic conductivity is typically given by[19]

$$\sigma_{\text{m}}^{\text{eff}} = \varepsilon_{\text{m}}^{\tau_{\text{m}}}(0.5139\lambda - 0.326)\exp\left[1268\left(\frac{1}{303} - \frac{1}{T}\right)\right] \qquad [1]$$

Note that $\sigma_{\text{m}}^{\text{eff}}$ is also related to the ionomer tortuosity τ_{m} and water content λ as well as temperature. Temperature variation is small between layers as justified before, while tortuosities and water content may vary from layer to layer: the former may arise from different fabrication techniques; the latter may be due to water transport characteristics. Water transport in the single-phase region (i.e., only gaseous phase in void space) is similar to the oxygen one, therefore a fairly small water content variation will be encountered across the dual layers. However, when liquid is present in pores, differences in porosity and other porous media properties, such as permeability and wetting characteristics between the two layers, may lead to discontinuity in the liquid saturation at the interface due to the fact that, typically, the capillary pressure is a function of the porous media properties and liquid saturation s (e.g., the Leverett function). This discontinuity can be estimated through equating capillary pressures at the two sides of the interface

$$P_{\text{c,I}} = P_{\text{c,II}} \Rightarrow \cos(\theta_{\text{c,I}})\left(\frac{\varepsilon_I}{K_I}\right)^{1/2} J(s_{\text{I}}) = \cos(\theta_{\text{c,II}})\left(\frac{\varepsilon_{\text{II}}}{K_{\text{II}}}\right)^{1/2} J(s_{\text{II}}) \qquad [2]$$

where $J(s)$ is the Leverett function. Note that the Leverett formula is developed for packed porous media while the catalyst layer contains both ionomer and carbon/catalyst particles that may lead to deviation. The above discussion also indicates that even without changing the ionomer content, the ionic conductivity can be different in the two-phase region by adjusting the properties of the porous electrode (e.g., electrode structure or wetting characteristics). Also the difference of saturations can be estimated by Eq. 2 or detected by advanced imaging techniques, such as X-ray or neutron imaging. Within each layer where properties are homogeneous, liquid saturation can be assumed uniform as justified in the single-layer electrode.[17] Liquid water dynamics in hydrophobic electrodes and its in situ characterization were conducted recently by Zhang et al.[20]

Difference in the specific area and exchange current density, $ai_{0,T}^{c,ref}$.— The catalyst specific area, a, describes the active catalyst surface area per unit volume, which is determined by factors such as the structural feature of the electrode (e.g., reaction interface roughness) and mean radius of the catalyst particles as well as the most important factor for catalyst cost reduction, Pt loading. The exchange current density $i_{0,T}^{\text{c,ref}}$ depends on factors such as temperature and the catalyst electrochemical characteristics. When liquid is

present in the pore, $ai_{0,T}^{c,ref}$ may decrease due to liquid coverage over the reaction interface and is typically given by[21,22]

$$ai_{0,T}^{ref,c} = ai_0^{ref,c}(1 - s)\exp\left[-\frac{E_a}{R_g}\left(\frac{1}{T} - \frac{1}{353.15}\right)\right] \quad [3]$$

where E_a denotes the activation energy for oxygen reduction reaction (ORR) at the Pt/Nafion electrode. As discussed previously, the saturation levels within the two layers may be different, therefore contributing to the difference in the value of $ai_{0,T}^{c,ref}$ in the two layers, while the temperature effect is negligible due to its small spatial variation. Furthermore, during a cold start, solid water may affect the electrode active area[23-25] and the modeling of ice impact typically follows the same way as the liquid one (i.e., Eq. 3). Because the volume fraction of solid water in the electrode is determined by the local reaction rate, therefore, even within each layer, $ai_{0,T}^{c,ref}$ may vary during a cold start, which complicates the analysis. In the following analysis, we exclude the cold start and focus on the main range of fuel cell operation (i.e., over the freezing point).

Analytical solutions.— In the dual-layer electrode (as shown in Fig. 2), we assume the oxygen concentrations, temperatures, electronic phase potential $\Phi^{(s)}$, and equilibrium potential U_o are the same between the two layers and uniform within each layer as justified in our previous analysis. Two major parameters are adjustable between the two layers: one is the ionic conductivity σ_m^{eff}, the other the product of specific active area and exchange current density $ai_{0,T}^{c,ref}$. In these two layers, the electrolyte phase potential, $\Phi^{(m)}$, at steady state can be modeled by

$$\text{For layer I:} \quad \nabla \cdot \left[(\sigma_m^{eff})_I \nabla \Phi_I^{(m)}\right] + j_I = 0$$

$$\text{For layer II:} \quad \nabla \cdot \left[(\sigma_m^{eff})_{II} \nabla \Phi_{II}^{(m)}\right] + j_{II} = 0 \quad [4]$$

where the transfer current density j is calculated through the Butler–Volmer equation, which is approximated by the Tafel kinetics due to the sluggish kinetics of the ORR

$$\text{For layer I:} \quad j_I = -(ai_{0,T}^{ref,c})_I\left(\frac{C_{O_2}}{C_{O_2}^{ref}}\right)\exp\left(-\frac{\alpha_c F}{R_g T}\eta\right)$$

$$\text{For layer II:} \quad j_{II} = -(ai_{0,T}^{ref,c})_{II}\left(\frac{C_{O_2}}{C_{O_2}^{ref}}\right)\exp\left(-\frac{\alpha_c F}{R_g T}\eta\right)$$

where

$$\eta = \Phi^{(s)} - \Phi^{(m)} - U_o \quad [5]$$

Note that Eq. 4 and 5 are the equations we also used in our previous analysis.[17] These equations are also vastly adopted by fuel cell modeling and numerical simulation[23-28] to integrate with descriptions of other transport processes. Validation[22,29,30] in terms of fuel cell performance has been done for fuel cell models that include Eq. 4 and 5.

Considering a one-dimensional (1D) domain as shown in Fig. 2, the governing equation for each layer can be written as

$$\text{For layer I:} \quad \frac{d^2}{dx^2}\Phi_I^{(m)} = \frac{(ai_{0,T}^{c,ref})_I}{(\sigma_m^{eff})_I}\frac{C_{O_2}}{C_{O_2}^{ref}} \times \exp\left[-\frac{\alpha_c F}{R_g T}\cdot(\Phi^{(s)} - U_o - \Phi_I^{(m)})\right] \quad [6]$$

$$\text{For layer II:} \quad \frac{d^2}{dx^2}\Phi_{II}^{(m)} = \frac{(ai_{0,T}^{c,ref})_{II}}{(\sigma_m^{eff})_{II}}\frac{C_{O_2}}{C_{O_2}^{ref}} \times \exp\left[-\frac{\alpha_c F}{R_g T}\cdot(\Phi^{(s)} - U_o - \Phi_{II}^{(m)})\right] \quad [7]$$

The boundary and interfacial conditions are set as

$$\Phi_I^{(m)} = \Phi_\delta^{(m)} \text{ and } \frac{d}{dx}\Phi_I^{(m)} = 0 \quad \text{at } x = \delta \quad [8]$$

$$\Phi_I^{(m)} = \Phi_{II}^{(m)} \text{ and } (\sigma_m^{eff})_I\frac{d}{dx}\Phi_I^{(m)} = (\sigma_m^{eff})_{II}\frac{d}{dx}\Phi_{II}^{(m)} \quad \text{at } x = \delta/2 \quad [9]$$

The solution to the above 1D problem can be explicitly given by For layer I:

$$\Phi_I^{(m)} - \Phi_\delta^{(m)} = \frac{R_g T}{\alpha_c F}\ln\{\Pi(\Delta U^{j_\delta}, \bar{x}) + 1\}$$

For layer II:

$$\Phi_{II}^{(m)} - \Phi_\delta^{(m)} = \frac{RT}{\alpha_c F}\ln\left\{\Psi\left(\Delta U^{j_\delta}, \frac{(\sigma_m^{eff})_I}{(\sigma_m^{eff})_{II}}, \frac{(ai_{0,T}^{c,ref})_I}{(ai_{0,T}^{c,ref})_{II}}\right) \cdot \left[\Pi\left(\Delta U^{j_\delta}, \frac{(\sigma_m^{eff})_I}{(\sigma_m^{eff})_{II}}, \frac{(ai_{0,T}^{c,ref})_I}{(ai_{0,T}^{c,ref})_{II}}, \bar{x}\right) + 1\right]\right\} \quad [10]$$

where

$$\Pi = \left\{\tan\left[\sqrt{\frac{\alpha_c F\Delta U^{j_\delta}}{2R_g T}\frac{(\sigma_m^{eff})_I}{(\sigma_m^{eff})_{II}}\frac{(ai_{0,T}^{c,ref})_{II}}{(ai_{0,T}^{c,ref})_I}\Psi\left(\Delta U^{j_\delta}, \frac{(\sigma_m^{eff})_I}{(\sigma_m^{eff})_{II}}\frac{(ai_{0,T}^{c,ref})_I}{(ai_{0,T}^{c,ref})_{II}}\right)}\cdot\left(\bar{x} - \frac{1}{2}\right)\right] - \tan^{-1}\sqrt{\frac{\Pi\left(\Delta U^{j_\delta}, \frac{1}{2}\right)}{\Psi\left(\Delta U^{j_\delta}, \frac{(\sigma_m^{eff})_I}{(\sigma_m^{eff})_{II}}\frac{(ai_{0,T}^{c,ref})_I}{(ai_{0,T}^{c,ref})_{II}}\right)}\frac{(\sigma_m^{eff})_I}{(\sigma_m^{eff})_{II}}\frac{(ai_{0,T}^{c,ref})_I}{(ai_{0,T}^{c,ref})_{II}}}\right\}^2 \quad [11]$$

and

$$\Psi = \Pi\left(\Delta U^{j_\delta}, \frac{1}{2}\right)\left[1 - \frac{(\sigma_m^{eff})_I}{(\sigma_m^{eff})_{II}}\frac{(ai_{0,T}^{c,ref})_I}{(ai_{0,T}^{c,ref})_{II}}\right] + 1$$

$$\Pi = \left\{\tan\left(\pm\left[-\frac{\alpha_c F}{2R_g T}\Delta U^{j_\delta}\right]^{1/2}(1 - \bar{x})\right)\right\}^2$$

Here, ΔU^{j_δ} is defined the same way as in Ref. 17, but based on the properties of layer I

$$\Delta U^{j_\delta} = R_{\delta,I} I^{j_\delta} \quad \text{where } I^{j_\delta} = -j_\delta\delta,\ R_{\delta,I} = \frac{\delta}{(\sigma_m^{eff})_I} \text{ and } j_\delta = j(x = \delta) \quad [12]$$

Note that even though $R_{\delta,I}$ is defined based on layer I's ionic conductivity, it is directly related to the overall resistance of the dual-layer electrode through the formula, $R_\delta = R_{\delta,I}/2(1 + (\sigma_m^{eff})_I/(\sigma_m^{eff})_{II})$. By substituting the solution of the electrolyte phase potential into Eq. 5, the transfer current density j can be expressed as

$$\text{For layer I:} \quad \frac{j_I}{j_\delta} = \Pi + 1$$

$$\text{For layer II:} \quad \frac{j_{II}}{j_\delta} = \frac{(ai_{0,T}^{c,ref})_{II}}{(ai_{0,T}^{c,ref})_I}\Psi(\amalg + 1) \qquad [13]$$

Note that at the interface of the two layers, (i.e., $x = \delta/2$), the transfer current densities become

$$j_{\delta/2,I} = j_\delta\left[\Pi\left(\Delta U^{j_\delta}, \frac{1}{2}\right) + 1\right]$$

and

$$j_{\delta/2,II} = j_\delta\frac{(ai_{0,T}^{c,ref})_{II}}{(ai_{0,T}^{c,ref})_I}\left[\Pi\left(\Delta U^{j_\delta}, \frac{1}{2}\right) + 1\right] \qquad [14]$$

When $(ai_{0,T}^{c,ref})_I \neq (ai_{0,T}^{c,ref})_{II}$, there exists discontinuity across the interface between the two layers. The magnitude of the discontinuity is proportional to the ratio of the products of specific active area and the exchange current density, $ai_{0,T}^{c,ref}$, in the two layers.

With the known distribution of $\Phi^{(m)}$, the reaction current contributed from each layer can be obtained through calculating the average current densities, I

$$\text{Layer I:} \quad \int_{0.5}^{1}|j(\bar{x})|d\bar{x} = I_{\delta/2} = -(\sigma_m^{eff})_I\frac{d\Phi_I^{(m)}}{d\bar{x}}\bigg|_{\bar{x}=1/2}$$

$$\text{Layer II:} \quad \int_0^{0.5}|j(\bar{x})|d\bar{x} = \int_0^1|j(\bar{x})|d\bar{x} - \int_{0.5}^1|j(\bar{x})|d\bar{x} = I_0 - I_{\delta/2}$$

$$= -(\sigma_m^{eff})_{II}\frac{d\Phi_{II}^{(m)}}{d\bar{x}}\bigg|_{\bar{x}=0} + (\sigma_m^{eff})_I\frac{d\Phi_I^{(m)}}{d\bar{x}}\bigg|_{\bar{x}=1/2} \qquad [15]$$

The current fluxes at the locations of $\bar{x} = 1/2$ and $\bar{x} = 0$ are calculated by substituting the profiles of the electrolyte phase potentials into Eq. 15

$$I_{\frac{\delta}{2}} = -(\sigma_m^{eff})_I\frac{d\Phi_I^{(m)}}{d\bar{x}}\bigg|_{\bar{x}=\frac{1}{2}} = \sqrt{2\frac{(\sigma_m^{eff})_I R_g T}{\alpha_c F}}\sqrt{j_\delta - j_{\frac{\delta}{2},I}}$$

$$I_0 = -(\sigma_m^{eff})_{II}\frac{d\Phi_{II}^{(m)}}{d\bar{x}}\bigg|_{\bar{x}=0} = \sqrt{2\frac{(\sigma_m^{eff})_{II}R_g T}{\alpha_c F}}\sqrt{j_{\delta/2,II} - j_0 + \frac{(\sigma_m^{eff})_I}{(\sigma_m^{eff})_{II}}(j_\delta - j_{\delta/2,I})} \qquad [16]$$

In Eq. 16, the average current I_0 can also be rearranged as a function of ΔU^{j_δ}

$$I_0 = \sqrt{2\frac{R_g T}{\alpha_c F}\frac{\Delta U^{j_\delta}}{R_{\delta,I}^2}}\sqrt{\frac{(ai_{0,T}^{c,ref})_{II}}{(ai_{0,T}^{c,ref})_I}\frac{(\sigma_m^{eff})_{II}}{(\sigma_m^{eff})_I}\left[\Psi\cdot\amalg(\Delta U^{j_\delta},0) - \Pi\left(\Delta U^{j_\delta}, \frac{1}{2}\right) + \Psi - 1\right] + \Pi\left(\Delta U^{j_\delta}, \frac{1}{2}\right)} \qquad [17]$$

A parameter can further be defined to compare the performances of the two layers

$$\beta_{21} = \frac{\int_0^{0.5}|j(\bar{x})|d\bar{x}}{\int_{0.5}^1|j(\bar{x})|d\bar{x}} = \frac{I_0 - I_{\delta/2}}{I_{\delta/2}} = \sqrt{\frac{(\sigma_m^{eff})_{II}}{(\sigma_m^{eff})_I}}\sqrt{\frac{j_{\delta/2,II} - j_0}{j_\delta - j_{\delta/2,I}} + \frac{(\sigma_m^{eff})_I}{(\sigma_m^{eff})_{II}}} - 1 \qquad [18]$$

In Eq. 18, the ratio of $ai_{0,T}^{c,ref}$ affects the value of β_{21} through the transfer current densities, j. Assuming a linear relation between $ai_{0,T}^{c,ref}$ and catalyst loading, another parameter can be defined to compare the catalyst utilizations in the two layers:

$$\beta_{21}^{Pt} = \frac{\beta_{21}}{\frac{(ai_{0,T}^{c,ref})_{II}}{(ai_{0,T}^{c,ref})_I}} = \frac{(ai_{0,T}^{c,ref})_I}{(ai_{0,T}^{c,ref})_{II}}\sqrt{\frac{(\sigma_m^{eff})_{II}}{(\sigma_m^{eff})_I}}\sqrt{\frac{j_{\delta/2,II} - j_0}{j_\delta - j_{\delta/2,I}} + \frac{(\sigma_m^{eff})_I}{(\sigma_m^{eff})_{II}}} \qquad [19]$$

Results and Discussion

Figure 3 shows the profiles of the overpotential variation $\Delta\eta$ or electrolyte potential variation $\Phi^{(m)}(\bar{x}) - \Phi_\delta^{(m)}$ in the cathode electrode at varying $(\sigma_m^{eff})_I/(\sigma_m^{eff})_{II}$. The properties of layer I are fixed, while the ones of layer II are set equal to those of layer I, except that the ionic conductivity may be different. Some properties can be found in Table I. The solid line is the baseline representing the single-layer electrode case, where the properties of the two layers are set the same. It can be seen that the overpotential variation deviates the single-layer curve when the ionic conductivity in layer II is changed. Increasing the ionic conductivity of layer II (i.e., lowering the ratio) will reduce the electrolyte phase potential variation across layer II, as shown in Fig. 3. Also at the lower ΔU^{j_δ}, changing $(\sigma_m^{eff})_I/(\sigma_m^{eff})_{II}$ has relatively smaller impact on the electrolyte phase potential profile. In addition, ΔU^{j_δ} is a lumped parameter that governs the electrolyte phase potential variation within single-layer electrodes, as discussed in our previous analysis[17] or within layer I in Fig. 3. It is also related to the overpotential variation or electrolyte phase potential variation within layer II.

Figure 4 displays the profiles of $\Delta\eta$ or $\Phi^{(m)}(\bar{x}) - \Phi_\delta^{(m)}$ in the electrode at different ΔU_δ and ratios of $(ai_{0,T}^{c,ref})_I/(ai_{0,T}^{c,ref})_{II}$. Similar to Fig. 3, varying $(ai_{0,T}^{c,ref})_I/(ai_{0,T}^{c,ref})_{II}$ leads to deviation from the single-layer curve in layer II. Lowering the value of $ai_{0,T}^{c,ref}$ in layer II (e.g., reducing the Pt loading) will diminish the electrolyte phase potential variation. This can be explained by the fact that lower $ai_{0,T}^{c,ref}$ causes smaller protonic current in layer II, which leads to smaller variation of the electrolyte phase potential.

Figure 5 shows the profiles of local transfer current densities at $\Delta U^{j_\delta} = 0.1$ V. It can be seen that the transfer current densities are continuous at the interface of the two layers on the ionic conductivity variation, while there exists a remarkable discontinuity when varying $ai_{0,T}^{c,ref}$. When lowering the ionic conductivity in layer II [i.e., the case of $(\sigma_m^{eff})_I/(\sigma_m^{eff})_{II} = 1.25$] and fixing the layer I's performance, the reaction rate in layer II increases due to the enlarged electrolyte phase potential variation or overpotential variation as shown in Fig. 3. Also when increasing $ai_{0,T}^{c,ref}$ in layer II, the reaction current jumps at the interface from layers I to II, as also indicated by Eq. 14. Figure 6 plots the local reaction rates at a lower ΔU^{j_δ} (i.e.,

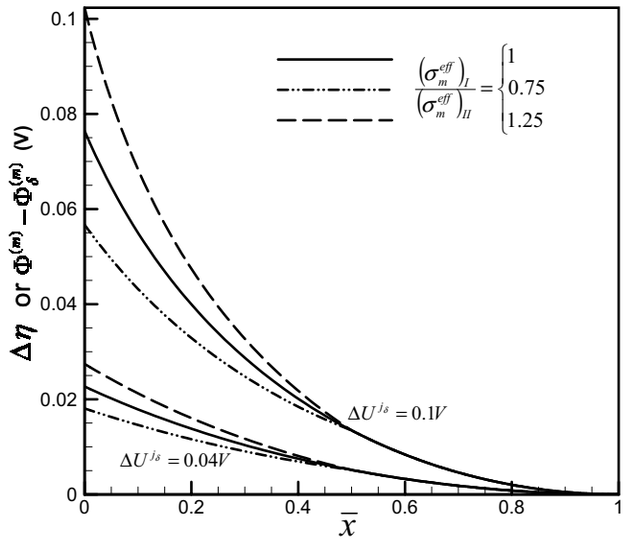

Figure 3. Profiles of $\Delta\eta$ or $\Phi^{(m)}(\bar{x}) - \Phi_\delta^{(m)}$ in the electrode at different ratios of σ_m^{eff}.

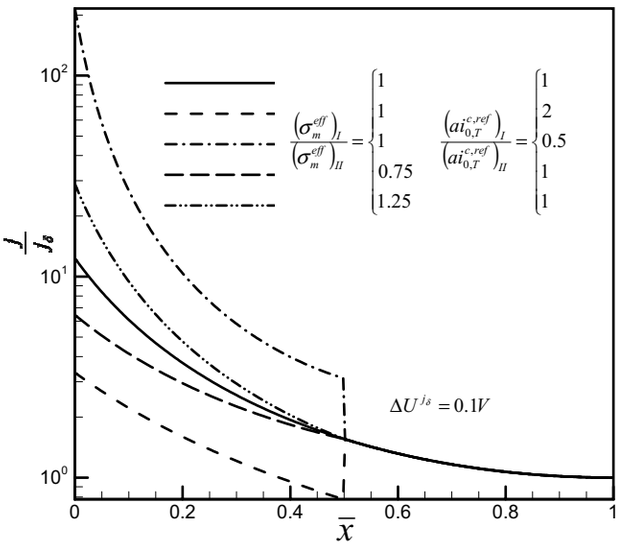

Figure 5. Profiles of the normalized local transfer current densities at varying $(ai_{0,T}^{\text{c,ref}})_{\text{I}}/(ai_{0,T}^{\text{c,ref}})_{\text{II}}$ and $(\sigma_{\text{m}}^{\text{eff}})_{\text{I}}/(\sigma_{\text{m}}^{\text{eff}})_{\text{II}}$ for $\Delta U^{j\delta}$ = 0.1 V.

$\Delta U^{j\delta}$ = 0.04 V). The trend is similar to the one in Fig. 5, except that the magnitudes of the variations are much smaller, which can be explained through Fig. 3 and 4.

The parameter $\Delta U^{j\delta}$ is directly related to the average current density I (or I_o) of the dual-layer electrode. Figure 7 gives the profiles of I vs $\Delta U^{j\delta}$ at $R_{\delta,\text{I}}$ = 0.00005 Ω m^2, or Eq. 17. As shown in Fig. 7, the average current density increases with $\Delta U^{j\delta}$ that lumps several parameters including oxygen concentration, electrode thickness, and surface overpotential. It can also be seen that $ai_{0,T}^{\text{c,ref}}$ has a significant impact on the profile and when its value doubles in layer II, the average current increases several fold at high $\Delta U^{j\delta}$. In addition, the average current density, I, is frequently used in the PEFC study. When the average current density is specified, $\Delta U^{j\delta}$ can be obtained from this figure or implicitly from Eq. 17, which can then be used to obtain the profiles of other quantities (e.g., Eq. 10). Furthermore, Fig. 7 also indicates that $\Delta U^{j\delta}$ around 0–0.1 V gives the typical range of fuel cell operation (i.e., I from 0 to 1.5 A/cm^2). Discussion on the cases at other R_δ can be found in our previous paper for single-layer electrodes.[17]

Figure 8 plots the profiles of β_{21} at varying $(ai_{0,T}^{\text{c,ref}})_{\text{I}}/(ai_{0,T}^{\text{c,ref}})_{\text{II}}$. β_{21} is defined to compare the performances of the two layers. Figure 8 indicates that the ratio of $ai_{0,T}^{\text{c,ref}}$ has profound impacts on the two layers' performances. When $\Delta U^{j\delta}$ is fixed, the value of β_{21} changes reversely with $(ai_{0,T}^{\text{c,ref}})_{\text{I}}/(ai_{0,T}^{\text{c,ref}})_{\text{II}}$, while at any fixed ratio of $ai_{0,T}^{\text{c,ref}}$, β_{21} increases rapidly with $\Delta U^{j\delta}$. At higher ratios of $ai_{0,T}^{\text{c,ref}}$ (e.g., lower Pt loading in layer II), the performance of layer II decreases however may still be larger than the layer I's (i.e., $\beta_{21} > 1$) at higher $\Delta U^{j\delta}$ (e.g., at higher average current densities, see Fig. 7).

Figure 9 shows the profiles of β_{21} at varying $(\sigma_{\text{m}}^{\text{eff}})_{\text{I}}/(\sigma_{\text{m}}^{\text{eff}})_{\text{II}}$. Similar to Fig. 8, the ratio of $\sigma_{\text{m}}^{\text{eff}}$ may significantly change the value of β_{21}. In addition, at low $\Delta U^{j\delta}$, the performances of the two layers are close (i.e., β_{21} is close to 1), while the difference becomes re-

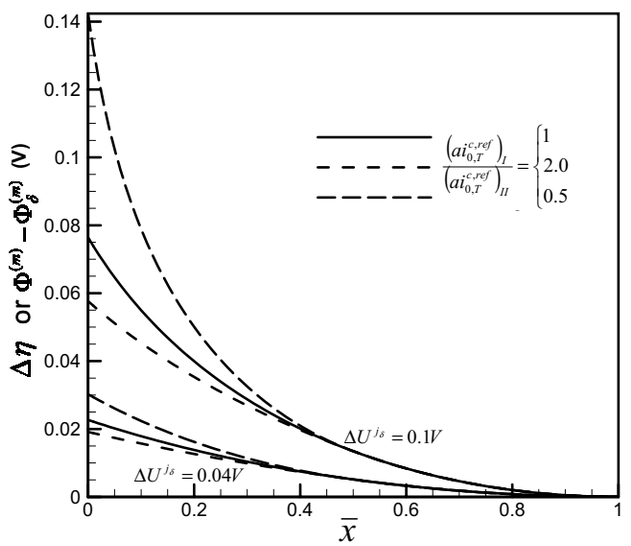

Figure 4. Profiles of $\Delta\eta$ or $\Phi^{(m)}(\bar{x}) - \Phi_\delta^{(m)}$ in the electrode at different ratios of $ai_{0,T}^{\text{c,ref}}$.

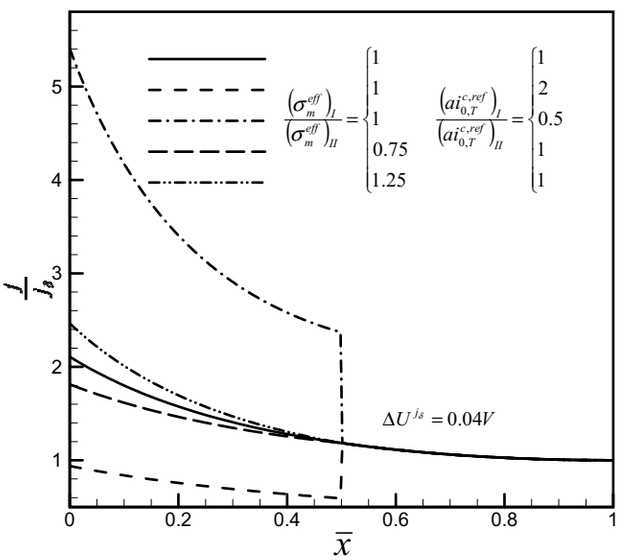

Figure 6. Profiles of the normalized local transfer current densities at varying $(ai_{0,T}^{\text{c,ref}})_{\text{I}}/(ai_{0,T}^{\text{c,ref}})_{\text{II}}$ and $(\sigma_{\text{m}}^{\text{eff}})_{\text{I}}/(\sigma_{\text{m}}^{\text{eff}})_{\text{II}}$ for $\Delta U^{j\delta}$ = 0.04 V.

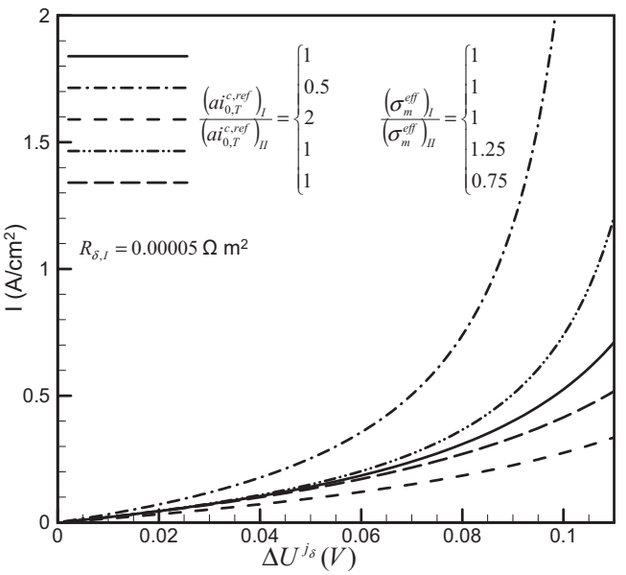

Figure 7. I vs $\Delta U^{j\delta}$ at varying $(ai_{0,T}^{c,ref})_I/(ai_{0,T}^{c,ref})_{II}$ and $(\sigma_m^{eff})_I/(\sigma_m^{eff})_{II}$.

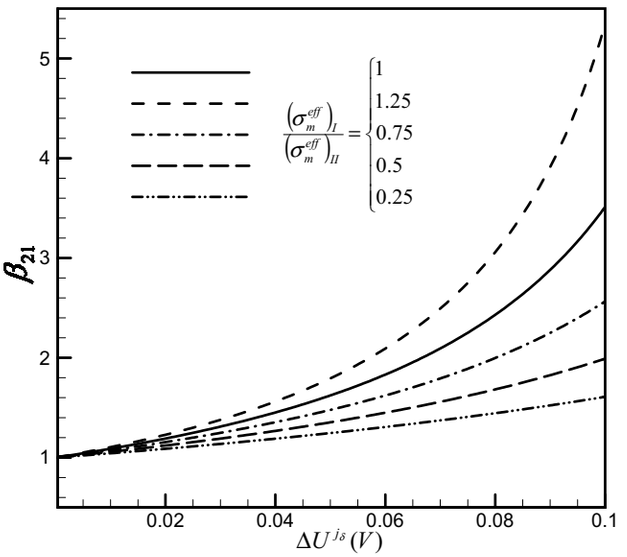

Figure 9. The profiles of β_{21} vs $\Delta U^{j\delta}$ at varying $(\sigma_m^{eff})_I/(\sigma_m^{eff})_{II}$ and $(ai_{0,T}^{c,ref})_I/(ai_{0,T}^{c,ref})_{II} = 1$.

markable as $\Delta U^{j\delta}$ increases. Different from the one of changing $ai_{0,T}^{c,ref}$, all the cases converge to one at low $\Delta U^{j\delta}$. In addition, increasing the ionic conductivity in layer II can make the two layers' performances close, but is unable to reduce β_{21} to <1 at high $\Delta U^{j\delta}$.

Figure 10 plots the profiles of β_{21}^{Pt} vs $\Delta U^{j\delta}$ at varying ratios of both parameters, which is similar to Fig. 9 in the way that all the curves converge to 1 at low $\Delta U^{j\delta}$. This can be explained by the fact that at low $\Delta U^{j\delta}$ (or either low current density or high ionic conductivity), the electrolyte phase potential variation is small and negligible; therefore, the local reaction rate is directly proportional to the value of local $ai_{0,T}^{c,ref}$ (see Eq. 5). In addition, increasing Pt loading in layer II will significantly promote the catalyst utilization ratio of layer II to layer I, while adding more Nafion in layer II will make the catalyst utilization more even between the two layers. Note that Fig. 9 also shows β_{21}^{Pt} profiles as $(ai_{0,T}^{c,ref})_I/(ai_{0,T}^{c,ref})_{II} = 1$.

Conclusions

This paper conducted a 1D analysis on the spatial variations of the key quantities including the electrolyte phase potential and reaction rate in PEFC cathode electrodes with two-layer configuration. Analytical solutions were obtained to explicitly describe the profiles of these quantities within the electrode as well as the two layers' performances. We also explored impacts of the important parameters, the ionic conductivity, specific surface area, and exchange current density, on each layer's performance. It found that reducing σ_m^{eff} and increasing the value of $ai_{0,T}^{c,ref}$ in layer II will enlarge the difference between the two layers' performances. Parameters of β_{21} and β_{21}^{Pt} were defined to quantify the ratios of the two layers' performances and catalyst utilizations, which are explicitly expressed as functions of the ratios of $ai_{0,T}^{c,ref}$ and σ_m^{eff} in the two layers. In addition, upon different $ai_{0,T}^{c,ref}$ in the two layers, there exists discon-

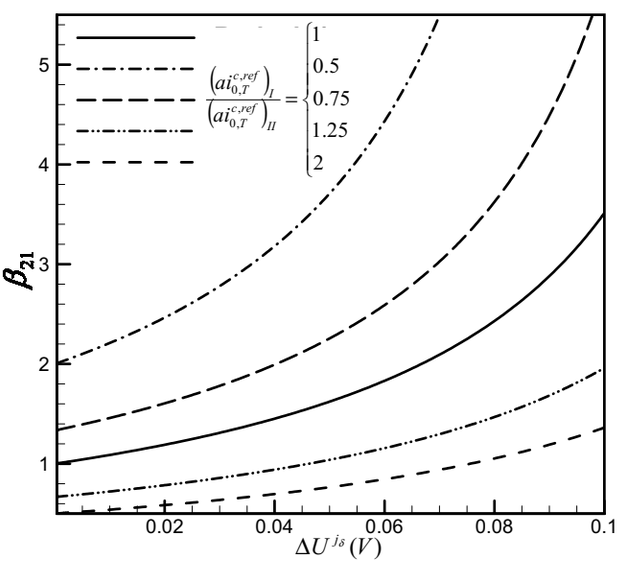

Figure 8. The profiles of β_{21} vs $\Delta U^{j\delta}$ at varying $(ai_{0,T}^{c,ref})_I/(ai_{0,T}^{c,ref})_{II}$ and $(\sigma_m^{eff})_I/(\sigma_m^{eff})_{II} = 1$.

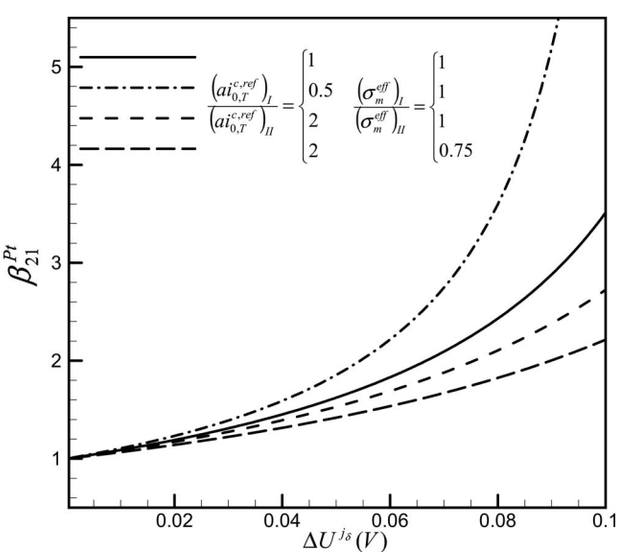

Figure 10. The profiles of β_{21}^{Pt} vs $\Delta U^{j\delta}$ at varying $(\sigma_m^{eff})_I/(\sigma_m^{eff})_{II}$ and $(ai_{0,T}^{c,ref})_I/(ai_{0,T}^{c,ref})_{II}$.

Table I. Physical parameters.

Quantity	Value
Exchange current density × reaction surface area in layer I, $ai_0^{ref,c}$	10,000 A/m^3
Volume fraction/Tortuosity of ionomer in electrodes in layer I, ε_m/τ_m	0.20/1.5
Transfer coefficient, α_c	1
O_2/H_2O molecular diffusivity in the cathode at standard condition, $D_{M,O_2,0}/D_{M,H_2O,0}$	$3.2348 \times 10^{-5}/3.89 \times 10^{-5}$ m^2/s
Temperature, T	353.15
Pressure, P	2 atm
Activation energy for oxygen reduction reaction, E_a	73,269 J/mol

tinuity in the reaction rate at the interface, while in the case that only σ_m^{eff} are changed, the reaction rate profiles are continuous. The exact solutions obtained by this paper can be applied to optimize the electrode performance through dual-layer configuration.

Acknowledgments

Partial support of this work by the SETsquared UK U.S. Collaborative Program is gratefully acknowledged.

The University of California, Irvine assisted in meeting the publication costs of this article.

List of Symbols

a	effective catalyst area per unit volume or specific area, m^2/m^3
C	molar concentration, mol/m^3
D	species diffusivity, m^2/s
F	Faraday's constant, 96,487 C/equivalent
I	current density, A/cm^2
i	superficial current density, A/cm^2
j	transfer current density, A/cm^3
k	thermal conductivity, W/m K
P	pressure, Pa
R	Ohmic resistance, mΩ cm^2
R_g	universal gas constant, 8.134 J/mol K
T	temperature, K
U_o	equilibrium potential, V

Greek

α	transfer coefficient
Φ	phase potential, V
σ	conductivity, S/m; surface tension, N/m
θ_c	contact angle, deg
λ	membrane water content
ε	porosity
η	surface overpotential, V
τ	tortuosity
δ	thickness, m

Superscripts and Subscripts

c	cathode; capillary
d	diffusion
eff	effective value
g	gas phase
m	membrane phase
ref	reference value
s	solid

References

1. S. S. Kocha, in *Handbook of Fuel Cells: Fundamentals, Technology and Applications*, W. Vielstich, H. Gasteiger, and A. Lamm, Editors, Vol. 3, John Wiley & Sons, Hoboken, NJ (2003).
2. M. K. Debe, in *Handbook of Fuel Cells: Fundamentals, Technology and Applications*, W. Vielstich, H. Gasteiger, and A. Lamm, Editors, Vol. 3, John Wiley & Sons, Hoboken, NJ (2003).
3. E. A. Ticianelli and E. R. Gonzalez, in *Handbook of Fuel Cells: Fundamentals, Technology and Applications*, W. Vielstich, H. Gasteiger, and A. Lamm, Editors, Vol. 2, John Wiley & Sons, Hoboken, NJ (2003).
4. C. Y. Wang, *Chem. Rev. (Washington, D.C.)*, **104**, 4727 (2004).
5. E. A. Ticianelli, C. R. Derouin, and S. Srinivasan, *J. Electroanal. Chem. Interfacial Electrochem.*, **251**, 275 (1988).
6. S. Mukerjee, S. Srinivasan, and A. J. Appleby, *Electrochim. Acta*, **38**, 1661 (1993).
7. O. Antoine, Y. Bultel, and P. Ozil, *Electrochim. Acta*, **45**, 4493 (2000).
8. E. Passalacqua, F. Lufrano, G. Squadrito, A. Patti, and L. Giorgi, *Electrochim. Acta*, **43**, 3665 (1998).
9. E. Antolini, L. Giorgi, A. Pozio, and E. Passalacqua, *J. Power Sources*, **77**, 136 (1999).
10. R. Madhusudana Rao and R. Rengaswamy, *Trans. Inst. Chem. Eng., Part A*, **84**, 952 (2006).
11. D. Song, Q. Wang, Z. Liu, T. Navessin, M. Eikerling, and S. Holdcroft, *J. Power Sources*, **126**, 104 (2004).
12. D. Song, Q. Wang, Z. Liu, M. Eikerling, Z. Xie, T. Navessin, and S. Holdcroft, *Electrochim. Acta*, **50**, 3347 (2005).
13. C. C. Boyer, R. G. Anthony, and A. J. Appleby, *J. Appl. Electrochem.*, **30**, 777 (2000).
14. P. K. Das, X. Li, and Z. S. Liu, *J. Electroanal. Chem.*, **604**, 72 (2007).
15. D. Lee and S. Hwang, *Int. J. Hydrogen Energy*, **33**, 2790 (2008).
16. P. P. Mukherjee and C. Y. Wang, *J. Electrochem. Soc.*, **154**, B1121 (2007).
17. Y. Wang and X. H. Feng, *J. Electrochem. Soc.*, **155**, B1289 (2008).
18. G. C. Li and P. G. Pickup, *J. Electrochem. Soc.*, **150**, C745 (2003).
19. T. E. Springer, T. A. Zawodzinski, and S. Gottesfeld, *J. Electrochem. Soc.*, **138**, 2334 (1991).
20. F. Y. Zhang, D. Spernjak, A. K. Prasad, and S. G. Advani, *J. Electrochem. Soc.*, **154**, B1152 (2007).
21. A. Parthasarathy, S. Srinivasan, and A. J. Appleby, *J. Electrochem. Soc.*, **139**, 2530 (1992).
22. Y. Wang, *J. Power Sources*, **185**, 261 (2008).
23. L. Mao and C. Y. Wang, *J. Electrochem. Soc.*, **154**, B341 (2007).
24. Y. Wang, *J. Electrochem. Soc.*, **154**, B1041 (2007).
25. H. Meng, *Electrochim. Acta*, **53**, 6521 (2008).
26. S. Mazumder and J. V. Cole, *J. Electrochem. Soc.*, **150**, 1503 (2003).
27. A. Z. Weber and J. Newman, *Chem. Rev. (Washington, D.C.)*, **104**, 4679 (2004).
28. A. Z. Weber and J. Newman, *J. Electrochem. Soc.*, **152**, A677 (2005).
29. H. Ju and C. Y. Wang, *J. Electrochem. Soc.*, **151**, A1954 (2004).
30. Y. Wang and C. Y. Wang, *Electrochim. Acta*, **51**, 3924 (2006).